Photodissociation of Nitrous Oxide Revisited by High-Resolution Photofragment Imaging: Energy Partitioning†

Tatsuhiro Nishide and Toshinori Suzuki*

Chemical Dynamics Laboratory, RIKEN, Wako 351-0198, Japan

Received: March 8, 2004; In Final Form: May 1, 2004

Energy partitioning in the 203−205 nm photodissociation of N_2O was studied by velocity map ion imaging of $O(^1D_2)$ and (2+1) resonance-enhanced multiphoton ionization (REMPI) of N_2 ($X^1\Sigma_g^+$) via the a″($^1\Sigma_g^+$) state. The observed translational energy distribution of O atoms exhibited a discrete structure due to quantized rotational energies of the counterpart N_2 fragments. The maximum of the N_2 rotational distribution has shifted from $J = 72$ to 74 in changing the photodissociation wavelength from 205.5 to 203.8 nm. Comparison of the translational energy distribution of $O(^1D_2)$ with the REMPI spectrum of N_2 ($X^1\Sigma_g^+$) revealed that the REMPI intensities of N_2 via particular rotational levels in the a″ state were specifically reduced. These rotational levels exhibited energy shifts due to perturbation, indicating that the REMPI efficiency is reduced by the interactions between the a″ state and other valence electronic state(s).

Introduction

Nitrous oxide is one of the most important greenhouse gases, and its reaction with $O(^1D_2)$ is the source of stratospheric NO that causes catalytic destruction of ozone. Nitrous oxide itself also produces $O(^1D_2)$ by photodissociation, $N_2O(^1\Sigma^+) + h\nu \rightarrow N_2(^1\Sigma_g^+) + O(^1D_2)$, in the UV window of the solar radiation (190−200 nm). These bimolecular and photochemical reactions act as important sinks in the global budget of N_2O.

Photodissociation of N_2O also plays a role in the isotope fractionation in the upper atmosphere.[1,2] For understanding this mechanism, Yung and Miller have considered the fact that the photoabsorption intensity of N_2O peaks at around 182 nm, and photodissociation in the UV window occurs in the red wing of this band.[3] The heavier isotopologues of N_2O with ^{15}N, ^{17}O, and ^{18}O atoms have smaller zero point energies, and, therefore, their spectra are slightly blue-shifted from that of the normal species, leading to smaller photoabsorption cross sections in the red wing. Thus, heavier isotopologues are more hardly decomposed by the UV radiation around 200 nm than the normal species and fractionated in the atmosphere.[3] Johnson and co-workers have further refined this model by taking account of the transition dipole moment that strongly depends on the bending angle of the molecule.[4] This dependence naturally arises because this particular UV absorption band is forbidden in nature and is induced by a breakdown of the Born−Oppenheimer approximation. Elucidation of the isotope fractionation process requires further detailed understanding of the photodissociation dynamics of N_2O, including the vibronic interactions.

Experimental studies on the UV photodissociation dynamics of N_2O have been performed with various experimental means. In 1991, Felder et al. reported photofragment translational spectroscopy (PTS) for 193 nm photodissociation, which revealed a singly peaked center-of-mass (COM) translational energy distribution of photofragments and a moderate but clearly positive angular anisotropy parameter ($\beta = 0.48 \pm 0.02$).[5] Springsteen et al. also studied the 193 nm photodissociation using VUV Doppler spectroscopy of $O(^1D_2)$ photofragments, which yielded $\beta = 0.50 \pm 0.05$.[6] In 1993, Hanisco and Kummel reported a one-color experiment, where a single laser (202−204 nm) was used to dissociate N_2O and detect N_2 fragments by resonance-enhanced multiphoton ionization (REMPI).[7] Their study revealed that the internal excitation of N_2 occurs almost exclusively in the rotational degree of freedom.

We have reported one-color two-dimensional (2D) photofragment imaging on 205.5 nm photodissociation of N_2O in 1996.[8] The $O(^1D_2)$ atoms were detected by two-photon excitation to the autoionizing $^1P_1$ state, and the alignment of the orbital angular momentum of $O(^1D_2)$ and its recoil speed dependence were observed. Since then, further imaging works on the photodissociation of N_2O have been reported. In 1999, Neyer et al. applied an improved photoion imaging method, so-called velocity mapping, to 203−205 nm photodissociation.[9,10] The anisotropy parameter was determined as a function of the J quantum number of N_2,[9] and the alignment of $O(^1D_2)$ was analyzed against its recoil speed.[10] Teule et al. have performed a similar work on the 203−205 nm photodissociation of the vibrationally excited N_2O molecule.[11] Ahmed et al. have observed an orbital alignment of $O(^1D_2)$ for 193 nm photodissociation.[12]

The first imaging work from this laboratory[8] was performed with an old technique using acceleration electrodes with meshes that limited the imaging resolution, while similar experiments were performed later in other laboratories with the velocity mapping technique that should provide superior resolution.[13,14] However, the resolution was still insufficient in that all of the observed $O(^1D_2)$ translational energy distributions were continuous and did not exhibit a discrete structure due to quantized rotational energies of the counterpart N_2 fragments. Close comparison of the reported $O(^1D_2)$ translational energy distributions and the REMPI spectrum of N_2 measured by Hanisco and Kummel[7] also revealed discrepancies in the peak position and the width.

To examine more closely the $O(^1D_2)$ translational energy distribution and the rotational distribution of N_2, this paper reports a velocity map ion imaging of the $O(^1D_2)$ fragment in

† Part of the special issue "Richard Bersohn Memorial Issue".

* Corresponding author. E-mail: toshisuzuki@riken.jp.

10.1021/jp048966a CCC: $27.50
Published on Web 06/25/2004

the 203−205 nm photodissociation of N_2O with higher resolution than previous works.

Experimental Section

The details of our laser system were described elsewhere.[15] Briefly, a Nd:YAG laser (Spectra Physics GCR230-25) was used to pump a commercial dye laser (Lumonics HD-500) and also a homemade power amplifier with a Bethune cell.[16] The output from the amplifier (80 mJ/pulse) was frequency-doubled in a KDP crystal, and the resulting second harmonic was mixed with the fundamental in a BBO crystal to produce the third harmonic. The phase-matching angles of the crystals were automatically tuned (Inrad Autotracker III) in scanning the dye laser wavelength. The third harmonic thus generated was separated from the fundamental and the second harmonic by reflecting the light with four dichroic mirrors. The laser beam was finally focused on the molecular beam with a lens ($f = 250$ mm). A typical laser power introduced into the chamber was 0.5−1.5 mJ/pulse. A single laser pulse served for both photodissociation of N_2O and ionization of the N_2 or $O(^1D_2)$ photofragments. Nitrogen molecules were ionized by (2+1) REMPI via the $a''(^1\Sigma_g^+)$ state at 203 nm, while $O(^1D_2)$ was ionized by two-photon excitation to the autoionizing $^1P_1$ state at 205.5 nm or the $^1F_3$ state at 203.8 nm. Because the (2+1) REMPI of N_2 exhibited rotational perturbations in the intermediate $a''(^1\Sigma_g^+)$ state, we determined the rotational energies in the a″ state accurately. For this purpose, the wavelength of the dye laser was calibrated with a pulsed wavemeter (Burleigh WA4500) and with atomic transitions of $O(^1P_1-{}^1D_2$, $^1F_3-{}^1D_2)$ and $Kr(2[^3/_2]2-{}^1S_0)$. While the laser wavelength was being scanned, a part of the fundamental light was sent through a monitor Etalon, and the transmitted laser intensity was measured simultaneously with the REMPI spectrum. The rotational line positions were determined using the observed Etalon fringes with the free spectral range of 0.247 cm^{-1}. The line width of our dye laser (fundamental) was 0.1−0.15 cm^{-1}.

A supersonic jet of N_2O was generated by a pulsed valve driven by a piezoelectric crystal in a source chamber and was collimated by a 2 mm diameter skimmer. We found that hot band absorption from the vibrationally excited level of N_2O cannot be neglected for the supersonic expansion of N_2O 20% in He, so we examined the vibrational cooling effect in different gas mixtures of 5% N_2O in Ar, 5% N_2O with 5% isobutane in Ar, and 2.5% N_2O with 10% isobutane in Ar. The stagnation pressure was kept at 1.5 atm. The vibrational cooling was examined by observing the ion images of state-selected N_2 fragments, as described later. We found the sample gas of 5% in Ar with 5% isobutane yielded the coldest vibrational temperature of N_2O in the beam, although the accurate temperature could not be determined in the present work All of the results presented in this paper were obtained with this sample gas. The enhanced vibrational cooling effect is ascribed to the low-frequency vibrational modes of isobutane that mediate the energy transfer from the vibrations of N_2O to the rotational and translational degrees of freedom. The molecular beam traveled through a buffer chamber and entered the main chamber through the second skimmer with an aperture of 1 mm. The source, buffer, and main chambers were evacuated by the 1400, 200, and 500 L/s turbo molecular pumps (Pfeiffer-Balzers, TMU1601, TMU262, and TMU521), respectively. The pressures were 10^{-5} and 10^{-8} Torr in the source and the main chamber in running the molecular beam, respectively.

The ions produced by REMPI were accelerated up to the kinetic energy of 2 keV and projected onto a dual microchannel plate (MCP) backed by a phosphor screen (P43) with an active area of 70 mm in diameter (Hamamatsu, F2226-24PGFX). A high voltage pulse that was 300 ns in duration was generated by a fast pulser (DEI, GRX3.0) and was applied to the MCP to time-gate the ions of interest. The transient image on the phosphor screen was observed through a viewing port and captured by a digital CCD camera (Hamamatsu, C8800-01, 1000 × 1000 pixels) with the readout rate of 30 frames/s. As an image intensifier usually limits the spatial resolution, it was not used in our setup. The electrodes for velocity mapping were of a new design proposed by Wrede et al.,[17] with our own small modification with several guard rings added between the original three electrodes. Although each microchannel of the MCP is 25 μm in inner diameter, each light spot on the phosphor screen becomes larger in size, and its image covers several pixels on a CCD chip. Therefore, real-time image processing was performed to calculate the center of gravity of each light spot with an accuracy of one pixel size of the CCD chip for resolution enhancement.[14,18] It was ascertained that light spots due to two different ions do not overlap each other, because otherwise these are counted as a single ion hit by the software. An observed ion image is 2D projection of the 3D scattering distribution of ions, and a slice through the 3D distribution was calculated by an inverse Abel transformation. The speed resolution Δv is constant over the speed range, and it was determined to be $\Delta v/v = 1.5-2.0\%$ from the ion images of state-selected N_2 fragments. The N_2 ion images were also used for determining the magnification factor of our velocity mapping setup and the aspect ratio of our imaging system. In the measurement of the REMPI spectrum, an AC component of a phosphor voltage was recorded using a fast preamplifier (NF, SA-230, 400 Hz to 140 MHz) and a box car integrator (Stanford Research Systems, SR450).

Because the REMPI detection of N_2 via the a″ state and $O(^1D_2)$ via the $^1F_3$ state is performed at very close laser wavelength, observed distributions can be compared directly. On the other hand, those between the REMPI of N_2 via the a″ state and $O(^1D_2)$ via the $^1P_1$ state are far apart by 2 nm, so the latter comparison provides the energy dependence of the dissociation dynamics.

Results

(a) $O(^1D_2)$ Fragment. Figure 1 shows the ion image of the $O(^1D_2)$ fragment measured by using two-photon excitation to the autoionizing $^1P_1$ state at 205.5 nm: the original 2D projection image is in (a), and a slice through the 3D scattering distribution is in (b). The ion images were measured by scanning the probe laser frequency to cover the Doppler-broadened atomic line. The laser polarization is in the vertical direction in the plane. The central vertical line seen in (b) is due to numerical noise caused by the inverse Abel transform and should be ignored. A discrete structure in the radial (recoil speed) distribution corresponds to quantized rotational energy levels of the counterpart N_2 fragments.

The discrete radial distribution is also seen in the ion image of $O(^1D_2)$ detected by excitation to the $^1F_3$ state at 203.8 nm (Figure 2). Comparison of Figures 1 and 2 reveals different image patterns; the angular distribution appears to be more isotropic in Figure 2. This, however, does not mean that photodissociation dynamics is different between the two cases. The difference of the image pattern originates from the fact that the REMPI detection of $O(^1D_2)$ via the $^1P_1$ and $^1F_3$ states has different sensitivities to the electronic orbital alignment ($v-J$ correlation) of $O(^1D_2)$, providing scattering angle-dependent

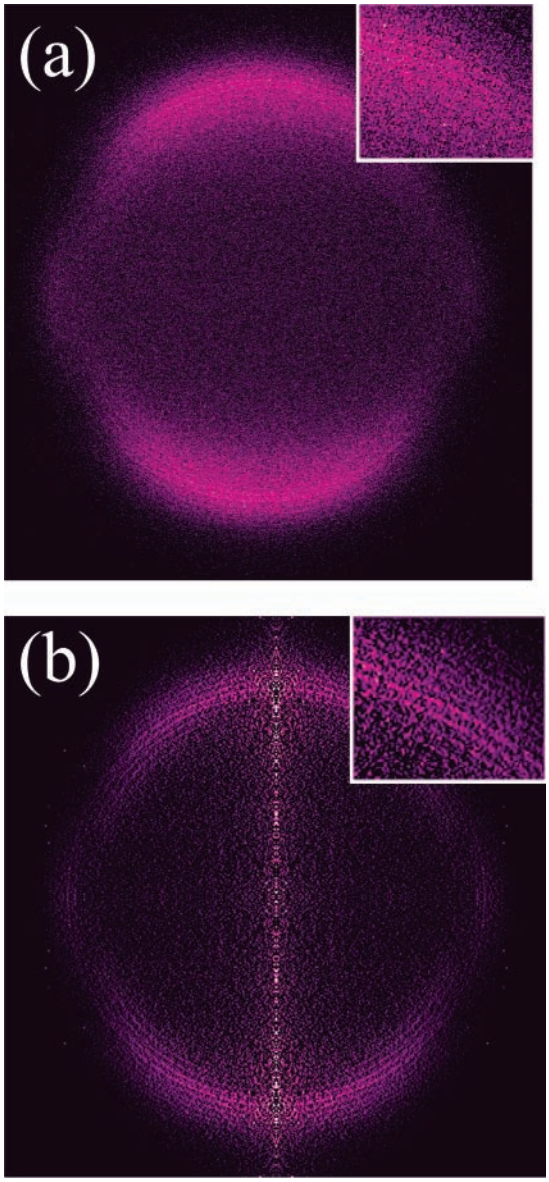

Figure 1. (a) The ion image of $O(^1D_2)$ observed by two-photon excitation to the $^1P_1$ state at 205.5 nm. The laser polarization is in the vertical direction in the figure. Integrated for 480 000 shots. (b) The slice through the 3D scattering distribution calculated from (a) using an inverse Abel transform.

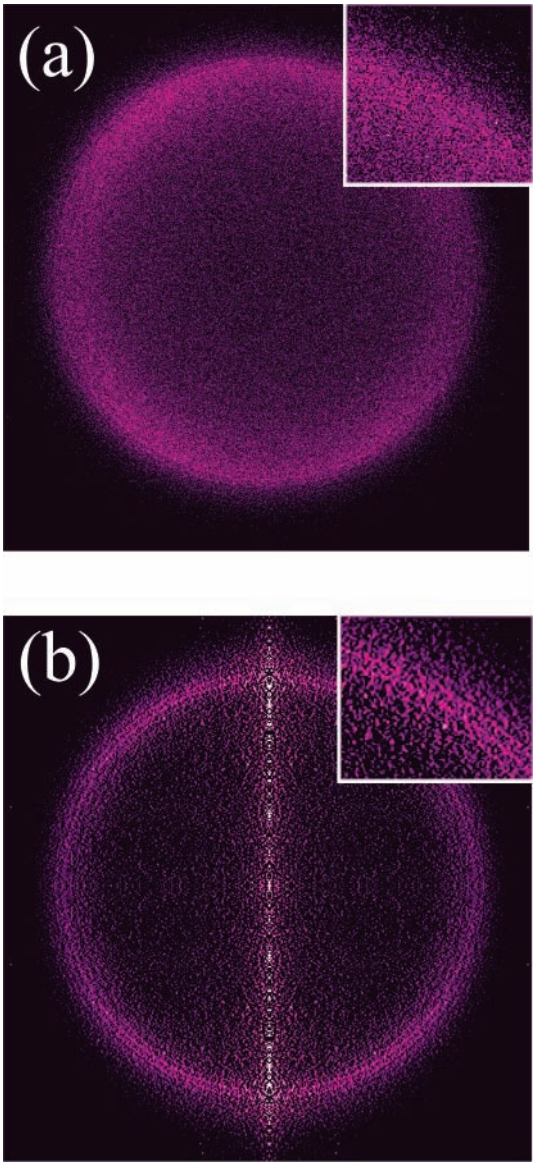

Figure 2. (a) The ion image of $O(^1D_2)$ observed by two-photon excitation to the $^1F_3$ state at 203.8 nm. The laser polarization is in the vertical direction in the figure. Integrated for 690 000 shots. (b) The slice through the 3D scattering distribution calculated from (a) using an inverse Abel transform.

detection efficiencies.[8,10−12,19] The analysis of the angular distributions in Figures 1 and 2 provides much information on the photodissociation dynamics but will be reported in detail elsewhere. The present work focuses on the radial distribution corresponding to the recoil speed of the $O(^1D_2)$ atoms.

By integrating the angular parts of the transformed images, the center-of-mass (COM) translational energy releases in photodissociation were calculated. The results are shown in Figure 3a and b with assignments of rotational quantum numbers of the counterpart N_2 fragments in $v = 0$. The absolute translational energies are quite similar between Figure 3a and b, indicating that an increased available energy in changing the photolysis wavelength from 205.5 to 203.8 nm has been effectively partitioned into the rotational energy of the N_2 fragment. Notice that the peak of the J distribution shifted from $J = 72$ to $J = 74$ in changing the photodissociation wavelength from 205.5 to 203.8 nm. The energy difference between the $J = 72$ and 74 rotational states in the $X^1\Sigma_g^+$ is 567 cm^{-1} that indeed exceeds the increased available energy, 396 cm^{-1}, in changing from 205.5 to 203.8 nm. The peaks observed in Figure 3 correspond to even J states of the N_2 fragment, and odd J states are between these peaks. The intensity alternation is due to the nuclear spin statistics of $^{14}N-^{14}N$ ($I = 1$) that provides a degeneracy that is 2 times larger in even J states than in odd J states.

It is interesting to examine whether the translational energy distribution varies with the scattering angle. For its examination, the COM translational energy distributions were extracted from the transformed images for the selected scattering angles of 5−15° and 85−95° with respect to the linear polarization of the laser, as presented in Figure 4. The case of ionization via the $^1P_1$ state is in (a) and via the $^1F_3$ state is in (b). In this analysis, the scattering angles of 0−5° were intentionally excluded from our consideration, as numerical noise caused by the inverse Abel transformation was rather large. Figure 4 shows that the translational energy releases are not largely different between the two regions of the scattering angle; however, a lower translational energy component seems to increase slightly at 90° than at 10° in Figure 4b.

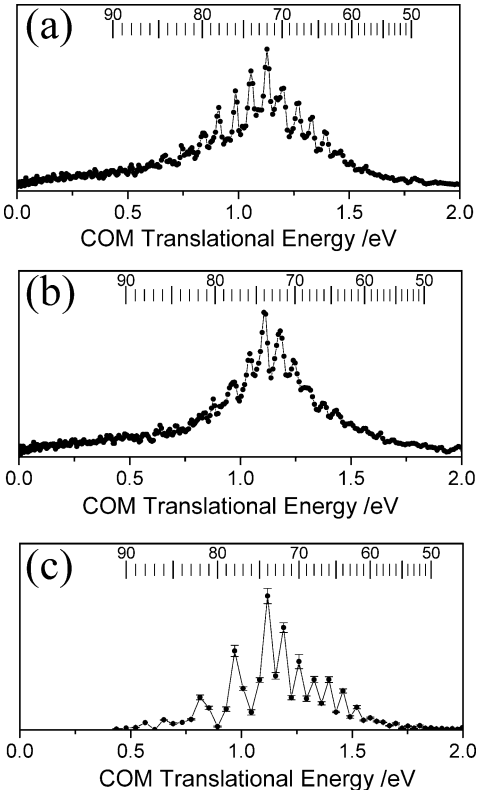

Figure 3. Center-of-mass translational energy releases in (a) 205.5 nm and (b) 203.8 nm photodissociation calculated from Figures 1 and 2, respectively. The sticks above the distributions indicate the translational energies expected for dissociation into $O(^1D_2)$ and N_2 ($v = 0$, J). For comparison, the rotational energy distribution of N_2 ($v = 0$) measured by (2+1) REMPI is shown in (c). Note that the photodissociation wavelength continuously changed in the measurement of (c) due to the nature of the one-color experiment, and the photodissociation energy varied by ~250 cm^{-1}. See Figure 5. The difference between (b) and (c) suggests that strong rotational perturbation exists in the a″ state of N_2.

(b) N_2 Fragment. Figure 5 shows the (2+1) REMPI spectrum of nascent N_2 ($X^1\Sigma_g^+$) produced by one-color 203 nm photodissociation of N_2O in a supersonic molecular beam. This spectrum corresponds to the Q-branch ($\Delta N = 0$) of the $a''(^1\Sigma_g^+) \leftarrow\leftarrow X(^1\Sigma_g^+)$ two-photon transition. The O- and S-branches are 2 orders of magnitude smaller in intensity than the Q-branch,[20] so they were not used in the present work. The intensity alternation of 2:1 due to nuclear spin statistics is clearly seen in the figure. The N_2 fragments are highly rotationally excited, and the distribution peaks at $J = 74$. Interestingly, the $J = 76$ line is clearly weaker than the adjacent ones. The overall spectral features are in excellent agreement with those reported by Hanisco and Kummel.[7] The line positions are listed in Table 1 where standard deviations derived from five independent spectra indicate the accuracy of our measurements.

Hanisco and Kummel have not assigned high J lines completely.[20] We initially followed the assignments by Rijs et al.,[21] and then we made our own assignments using ion imaging of N_2 fragments in each quantum state. The kinetic energy of a state-selected N_2 fragment can be related to the rotational energy of N_2 with the following energy conservation law:

$$E_{trans}(v,J) = h\nu - D_0 - \{E_{vib}(v) + B_v J(J+1) - D_v J^2(J+1)^2\} + E_{int} \quad (1)$$

where D_0 is the bond energy, E_{vib} is the vibrational energy, and

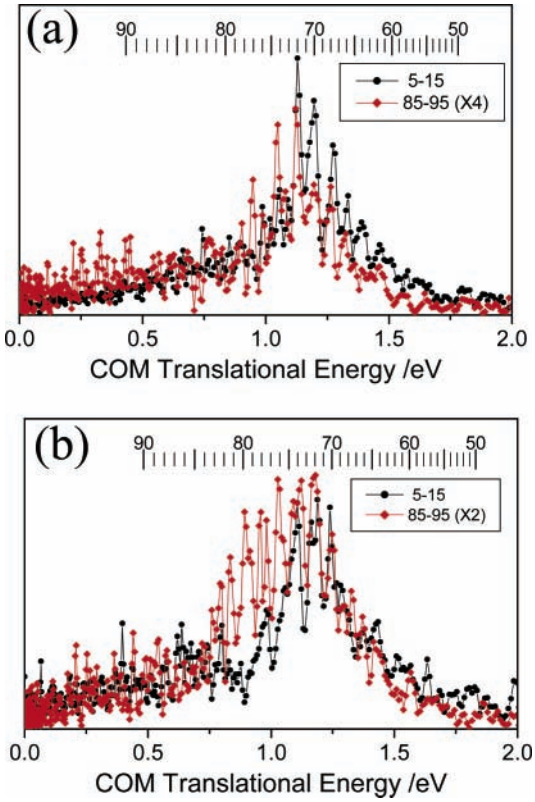

Figure 4. Center-of-mass translational energy releases calculated from the ion images for the specific scattering angles of 5−15° (black) and 85−95° (red) in (a) 205.5 nm and (b) 203.8 nm. The sticks above the distributions indicate the translational energies expected for dissociation into $O(^1D_2)$ and N_2 ($v = 0$, J). The intensities at 85−95° are magnified to allow close comparison with the distributions at 5−15°.

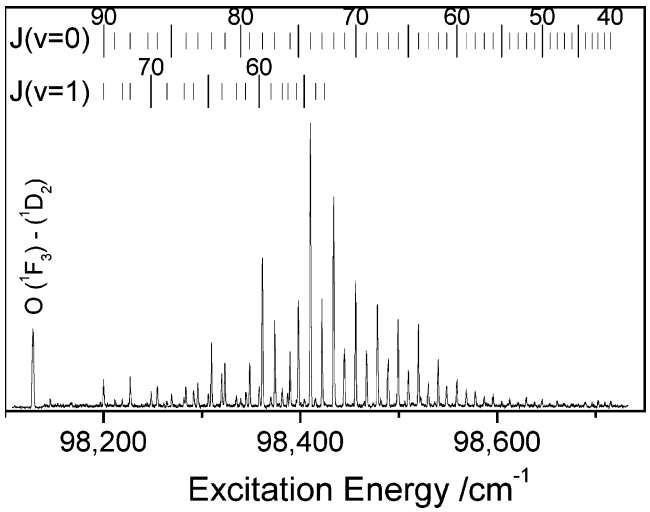

Figure 5. The (2+1) REMPI spectrum of nascent N_2 in the one-color photodissociation/detection experiment of N_2O in a supersonic molecular beam. The spectrum shows a Q-branch ($\Delta N = 0$) of the two-photon transition of $a''(^1\Sigma_g^+) \leftarrow\leftarrow X(^1\Sigma_g^+)$. The rotational assignments are indicated by vertical lines above the spectrum. Note that lines are missing, $J = 63$, 67, and 72 of the $v'-v'' = 1-1$ transition. See also Table 1.

B_v and D_v are the vibrational-state-dependent rotational and centrifugal distortion constants in the ground electronic state of N_2. E_{int} is the internal energy of N_2O in the ground state and is zero for photodissociation from the (000) level. Therefore, the rotational quantum numbers were determined from the ion images observed by fixing the laser frequency on each rotational line.

TABLE 1: Q-Branch of the a″−X Band of N_2[a]

	$v = 0$		$v = 1$	
J	obs. (cm^{-1})	σ	obs. (cm^{-1})	σ
40	98 715.56	0.22		
41	98 709.15	0.29		
42	98 702.75	0.14		
43	98 696.18	0.24		
44	98 689.39	0.14		
45	98 682.34	0.27		
46	98 675.48	0.34		
47	98 668.08	0.08		
48	98 660.75	0.30		
49	98 653.00	0.38		
50	98 645.28	0.24		
51	98 637.64	0.42		
52	98 629.48	0.09		
53	98 621.36	0.19	98 425.13	0.22
54	98 612.75	0.11	98 415.23	0.11
55	98 604.67	0.09	98 404.28	0.08
56	98 595.66	0.18	98 397.32	0.70
57	98 586.81	0.07	98 387.27	0.09
58	98 577.71	0.10	98 381.70	0.09
59	98568.45	0.16	98 370.04	0.08
60	98 559.05	0.16	98 358.30	0.10
61	98 548.71	0.13	98 345.06	0.09
62	98 539.97	0.12	98 335.17	0.11
63	98 529.96	0.09		
64	98 519.92	0.09	98 320.12	0.10
65	98 509.62	0.08	98 306.58	0.11
66	98 499.12	0.06	98 291.64	0.05
67	98 489.27	0.06		
68	98 478.19	0.07	98 281.69	0.19
69	98 467.24	0.02	98 264.36	0.16
70	98 456.07	0.03	98 248.37	0.11
71	98 444.65	0.06	98 227.23	0.10
72	98 434.00	0.08		
73	98 422.06	0.07	98 218.74	0.14
74	98 410.21	0.07	98 200.24	0.06
75	98 398.03	0.08		
76	98 389.70	0.04		
77	98 374.12	0.06		
78	98 361.43	0.08		
79	98 348.49	0.09		
80	98 339.46	0.08		
81	98 323.24	0.10		
82	98 309.72	0.11		
83	98 295.67	0.11		
84	98 283.78	0.12		
85	98 269.20	0.11		
86	98 254.70	0.10		
87	98 243.97	0.30		
88	98 227.23	0.10		
89	98 211.69	0.17		
90	98 200.24	0.06		
91	98 182.91	0.08		

[a] σ is the standard deviation calculated from five spectra measured independently.

In determining the translational energy of a state-selected N_2 fragment, care was taken to discriminate photodissociation from the (000) and (010) levels in the ground electronic state of N_2O. Due to the nature of the linear-bent transition of this particular UV absorption band, where the forbidden transition is allowed by bending distortion, the transition from the excited bending level in the ground electronic state, (010), is expected to be rather strong. In our previous work on OCS that is isovalent with N_2O, we found that photoabsorption from (010) is more than 7 times stronger than that from the (000) level.[22] A similarly large photoabsorption intensity from the (010) level is anticipated for N_2O. Johnson and co-workers have estimated that the relative transition strength from the (010) level of N_2O at room temperature is comparable to or greater than that from (000) at

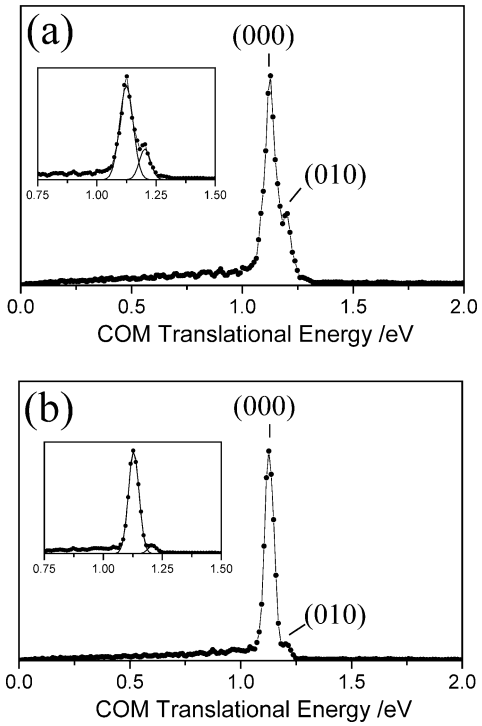

Figure 6. The translational energy distribution of the N_2 fragment in a single quantum state of $v = 0$ $J = 74$. Different sample gas mixtures, (a) 20% N_2O in He and (b) 5% N_2O in Ar with 5% isobutane, were used. The main peak is due to photodissociation starting from the zero vibrational level in the ground state, while the shoulder on the high energy side is from the excited bending level (010). The smaller intensity of the shoulder in (b) reflects a colder vibrational temperature.

205.5 nm.[4] Due to an incomplete vibrational cooling in a supersonic free jet carried by rare gases, a population remains in the (010) level even in a supersonic molecular beam. Figure 6 shows translational energy distributions of the N_2 fragment in the single quantum state of $v = 0$ and $J = 74$ measured for different molecular beam conditions of (a) 20% in He and (b) 5% in Ar with 5% isobutane. In both cases, the main peak is due to photodissociation starting from the (000) level of N_2O (cold band), while a shoulder appearing on the high energy side is from the (010) level of N_2O (hot band). The vibrational energy of the latter state is 589.2 cm^{-1},[23] and this additional vibrational energy appears as the larger translational energy release. The hot band intensity clearly diminished in (b). Thus, we have used isobutane to enhance vibrational cooling in a supersonic free jet expansion throughout the present work. We performed least-squares fitting of two Gaussian functions to the observed translational energy distributions for correctly evaluating the translational energy of N_2 in photodissociation starting from the (000) level of N_2O. The qualities of these fits are presented in the insets in Figure 6.

The center frequency of each rotational line was accurately determined by the least-squares fitting of the line profile using a Gaussian function. The Gaussian function was employed, because the N_2 fragments are predominantly scattered perpendicular to the $\boldsymbol{k}$ vector of the laser beam, which provides parabolic line shapes. The laser bandwidth was about 0.l−0.15 cm^{-1} in the fundamental at 610 nm and effectively 0.6−0.9 cm^{-1} in the two-photon absorption of its third harmonic. Therefore, no fine structure was observed in the Doppler profile. Although the absolute line positions we determined differ by 1−1.5 cm^{-1} from those by Rijs et al.,[21] the spectral assignments of the $v'-v'' = 0-0$ lines mostly agreed. Using the rotational and centrifugal constants of $B_0'' = 1.9895924(30)$ and $D_0'' =$

TABLE 2: Rotational Constants in the $a''^1\Sigma_{g^+}$ ($v' = 0$) State of N_2

constants	this work	ref 20	refs 24 and 25	ref 21
ν_{00}	98 840.10(26)	98 840.59(12)	98 840.55(8)[a]	98 840.41(9)
B_0	1.91429(12)	1.9143(2)	1.913748(42)[b]	1.91439(4)
$D_0 \times 10^6$	6.133(12)	6.6(2)	6.088(99)[b]	6.143(2)

[a] Reference 24. [b] Reference 25.

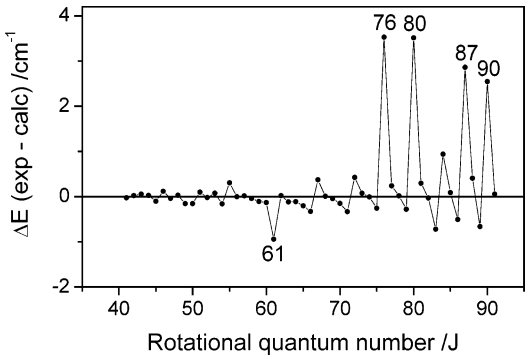

Figure 7. Energy shifts of the rotational levels of the $v = 0$ state in the a″ electronic state from the expected value using $\nu_{00} = 98\,840.10$, $B_0' = 1.91429$, and $D_0' = 6.133 \times 10^{-6}$ cm^{-1}.

5.7606(76) $\times$ 10^{-6} cm^{-1} that are accurately known for the ground electronic state, the rotational and the centrifugal constants in the a″ state were determined from the Q-branch line positions of $J = 40-91$ as summarized in Table 2. The term value of the $(v',J') = (0,0)$ level in the a″ state was determined to be $\nu_{00} = 98\,840.10(26)$ cm^{-1}, and B_0' and D_0' were 1.91429(12) and 6.133(12) $\times$ 10^{-6} cm^{-1}, respectively. Previously, Yoshino and Freeman[24] have estimated the term value of the $a''(v',J') = (0,0)$ state to be 98 840.55 $\pm$ 0.08 cm^{-1} by combining the results of their VUV spectroscopy of the $c_5'(0)^1\Sigma_u^+-X^1\Sigma_g^+$ and $c_4(0)^1\Pi_u-X^1\Sigma_g^+$ bands and visible spectroscopy of the $c_5'(0)^1\Sigma_u^+-a''^1\Sigma_g^+$ and $c_4(0)^1\Pi_u-a''^1\Sigma_g^+$ bands reported by Suzuki and Kakimoto.[25] Considering the fact that our ν_{00} was determined by the least-squares fit of the $J = 40-91$ line positions of the Q-branch that are far from Q(0), the observed agreement with the value reported earlier by Yoshino and Freeman is remarkably good. From an analysis of (2+1) REMPI, Haniso and Kummel[20] and Rijs et al.[21] have obtained the values listed in Table 2.

The energy shifts of the observed levels from the expectation values of $E_{rot} = B_vJ(J+1) - D_vJ^2(J+1)^2$ are plotted in Figure 7, which is in qualitative agreement with the work of Rijs et al.[21] Clear signatures of rotational perturbation are seen for $J = 61$, 76, 80, 87, and 90. These rotational levels were excluded from the least-squares fit in obtaining the B_0' and D_0' constants. Higher-order centrifugal corrections were not necessary, as Rijs et al. have already pointed out.[21] The differences between the observed and calculated rotational energies in the a″ state are smaller in our result in Figure 7 than in Figure 2a in Rijs et al.:[21] the deviation of rotational energies from the expected values is less than 0.5 cm^{-1} for $J = 40-75$, except for $J = 61$ in our results.

The rotational perturbation is stronger in the $v' = 1$ state, and it even washes out the 2:1 intensity alternation in REMPI. Therefore, the assignment of the $v'-v'' = 1-1$ lines were more difficult to perform than that of 0−0. We determined the J'' quantum numbers from the translational energies of the state-selected N_2 fragments, which provided different assignments for the 1−1 lines from those by Rijs et al.,[21] who extended the assignments of low J lines by Hanisco and Kummel.[20] Typically, assigned J' numbers are lower by 2 in our result than those by

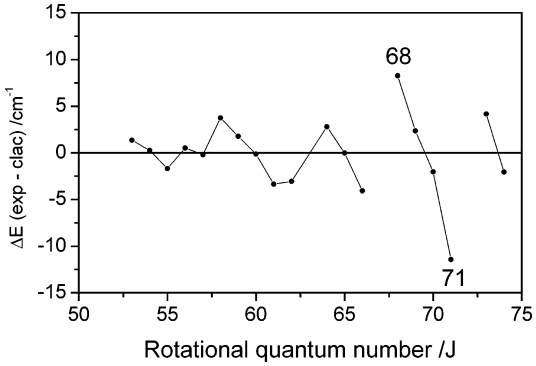

Figure 8. Energy shifts of the rotational levels of the $v = 1$ state in the a″ electronic state from the expected value using $\nu_{11} = 98\,655.3$, $B_1' = 1.8921(8)$, and $D_1' = 6.0(2) \times 10^{-6}$ cm^{-1}.

Rijs et al.[21] Using our assignments and the value of $\nu_{11} = 98\,655.3$ cm^{-1} reported by Hanisco and Kummel,[20] we obtained the B_1' and D_1' constants for the $v' = 1$ state in the a″ electronic state as 1.8921(8) and 6.0(2) $\times$ 10^{-6} cm^{-1}, respectively. As indicated in Figure 8, the energies of all rotational states in $v' = 1$ are scattered around the values calculated using the B_1' and D_1' constants.

For extraction of the rotational state distribution of N_2, the two-photon line strength in the a″−X transition of N_2 must be considered. It has been shown that the Q-branch of this particular transition barely depends on the rank 2 and rank 4 alignment parameters,[26] and this correction is expected to be less than 10% in the transition intensity. Thus, we approximated that the line strength from each (J, m_J) quantum state is independent of m_J and regarded the observed REMPI line intensities (peak areas) as the rotational population of N_2 in each J state directly.

The nascent rotational distribution of N_2 thus determined is shown in Figure 3c. Notice that, due to the nature of the one-color photodissociation/detection experiment, the photodissociation wavelength continuously varied in scanning the laser frequency to detect N_2 fragments. However, the variation of the available energy (250 cm^{-1}) is sufficiently small to neglect for the purpose of our discussion. There are clear discrepancies between Figure 3b and c in the intensities at particular J states such as $J = 76$ and 80 of the N_2 fragment. This suggests that the REMPI intensity of N_2 is suppressed at these J states.

Discussion

(a) Comparison between Translational Energy Distribution of $O(^1D_2)$ and Rotational Distribution of N_2. The observed translational energy distribution of $O(^1D_2)$ is essentially a bell shape, except for the intensity alternation due to the nuclear spin statistics of N_2, while the rotational distribution of N_2 extracted from the REMPI spectrum exhibits clear dips at some rotational states such as $J = 76$. As seen in Figure 7, the rotational levels in the a″ state that exhibit reduced REMPI intensities are subject to large energy shifts. Thus, we conclude that the anomalies in the REMPI intensities are due to the coupling of the intermediate a″ state with other electronic states that are hardly ionized. The perturbing state is not identified yet; however, it must be a valence state, because the a″ state is the lowest member of the Rydberg states converging to the ground electronic state of N_2^+.

Umemoto has reported that the REMPI signal of $^{14}N_2$ was weaker than that of $^{14}N^{15}N$ in the photodissociation of $^{14}N_2{}^{16}O$, $^{14}N^{15}N^{16}O$, and $^{15}N^{14}N^{16}O$, from which Umemoto suggested that predissociation occurs from the intermediate state of REMPI.[27] It implies that, even though large energy shifts are seen only

for particular J' states as shown in Figure 7, quenching may be present at all rotational levels in the a″ state.

(b) Bond Energy. The ion images of state-selected $N_2(v = 0)$ fragments were used to determine the magnification factor of our velocity mapping setup, which also provided an estimate for the bond energy. The square of the radius (speed) of an ion image is proportional to the translational energy provided by eq 1. With the rotational and centrifugal constants fixed to the literature value, the magnification factor and the bond energy were set as unknown parameters to determine the least-squares fit. In this analysis, we have taken account of the variation of the photodissociation wavelength in observing different J states of the N_2 fragments due to the nature of the one-color experiment. The bond dissociation energy that minimizes the difference between the observed and calculated $E_{trans}(0,J)$ for the state-selected N_2 fragments was found to be 3.629(5) eV, which is slightly smaller than the value of 3.639(5) eV calculated from the heat of formation.[23] The results of the $N_2(v = 1)$ fragments were not used in the analysis, as the rotational assignments of the $v'-v''=1-1$ band were more difficult due to stronger perturbation to the $v' = 1$ level in the a″ state. The magnification factor determined from the $N_2(v = 0)$ fragments was used to assign the rotational lines of the $v'-v'' = 1-1$ band as described above.

(c) A′ and A″ States. The first absorption band of the 16 valence electron systems such as N_2O and OCS is predominantly due to electronic transitions to the A′ Renner−Teller component of the $^1\Delta$ state from the ground electronic state.[28,29] This transition is forbidden in the linear geometry but is weakly allowed in the bent geometry. The transition dipole moment is only slightly off the molecular axis in the linear geometry, providing a large positive anisotropy parameter in the photofragment angular distributions. Because the upper state surface has a steep slope toward the bent geometry, a strong torque exerts on the diatomic fragment in the dissociation process, resulting in extremely strong rotational excitation in the diatomic fragment. The vibrational degree of freedom in the diatomic fragment is essentially a spectator during the reaction. The diabatic potential energy surface of the A′($^1\Delta$) state is not dissociative; however, a conical intersection with a repulsive A′($^1\Pi$) state makes the adiabatic surface dissociative. The A″-($^1\Delta$) state is located much higher in energy and plays no role in the dissociation process of N_2O at 203−205 nm.

There is another electronic state, A″($^1\Sigma^-$), that carries an oscillator strength from the ground state in this region. The difference between the A′($^1\Delta$) and A″($^1\Sigma^-$) states is that the electron hole is in the out-of-plane π orbital in the former while it is in the in-plane π orbital in the latter. Having the same π^* electron, the topographies of the A′ and A″ surfaces are quite similar to each other.

The dipole moment of the transition to A″($^1\Sigma^-$) is perpendicular to the molecular plane; therefore, photodissociation from the A″ state provides the photofragment anisotropy parameter β_2 of −1.0. On the other hand, the anisotropy in dissociation from the A′ state depends on the relative angle of the transition dipole moment with respect to the molecular axis in the ground state, which is not known accurately. However, we may assume β_2 in dissociation from the A′ state to be 1.8, in analogy with the OCS case.[29] The anisotropy parameter measured for the N_2 fragments was about 1.0, indicating that photodissociation occurs from both the A′ and the A″ states. Assuming a β_2 of 1.8 and −1 for dissociation from the A′ and A″ states, respectively, the observed anisotropy parameter provides the estimate for the relative contribution of the A′ state, x, as follows:

$$\beta_{obs} = x(1.8) + (1 - x)(-1) = 1.0$$

This equation provides $x = 0.71$. In other words, the contribution of the dissociation from the A′ state is 70%. The theoretical estimate[30] on the contribution of the dissociation from the 2A′-($^1\Delta$) state was 97%, which is likely to be an overestimation.

As presented in Figure 4, the radial distribution in the inverse Abel transformed image seems slightly different between the scattering angles of 10° and 90°. The scattering to the former angle is primarily due to dissociation from the A′ state, while to the latter angle it is due from the A″ state. Two possible reasons may be considered as the source of the slight difference in radial distribution. One is that the COM translational energy release, or the strength of rotational excitation in the N_2 fragment, is indeed different between the two dissociation channels. This implies that the bending potentials of the A′ and A″ states are slightly different from each other. An alternative explanation against this idea is that the electronic orbital alignment of $O(^1D_2)$ rapidly varies with the rotational quantum number J of the counterpart N_2 fragment, and the radial distributions at 10° and 90° are no longer proportional to the real speed distributions (flux distributions) of $O(^1D_2)$ (= the rotational distribution of N_2) at individual scattering angles. We speculate the former is more likely, although the latter cannot be completely excluded at this point. Extensive analysis of the orbital alignment of $O(^1D_2)$ is necessary to completely elucidate this problem.

Examination of the recoil speed dependence of the orbital alignment of $O(^1D_2)$ is rather difficult to perform with the one-color photodissociation/detection arrangement. Previously, Neyer and co-workers have attempted to determine the orbital alignment of $O(^1D_2)$ corresponding to each J state of N_2 by comparing one-color experiments at 203.8 and 205.5 nm, as the REMPI of $O(^1D_2)$ at these wavelengths via $^1F_3$ and $^1P_1$ provided different sensitivities to the orbital alignment.[9] Our high-resolution data have shown that photodissociation at 203.8 and 205.5 nm results in the N_2 rotational distributions with their maxima being different by two quanta of J. Is dissociation dynamics at the two different dissociation wavelengths sufficiently similar to combine the results for determining the orbital alignment of $O(^1D_2)$? If so, should we compare the angular distributions of $O(^1D_2)$ at these laser wavelengths for the same recoil speed of $O(^1D_2)$ or the same J quantum number of the counterpart N_2 (i.e., the different recoil speeds of O atoms)? Such ambiguities arise from the nature of the one-color experiment.

Conclusion

The energy partitioning in 203−205 nm photodissociation of N_2O has been studied by velocity map ion imaging of the $O(^1D_2)$ and N_2 photofragments and (2+1) REMPI spectroscopy of N_2. The $O(^1D_2)$ ion images were obtained with the resolution much higher than previous works, where the rotational levels of the counterpart N_2 fragment were resolved as discrete translational energies of the O atoms. The spectroscopic assignments of the a″ ← ← X two-photon transition of N_2 were performed with the help of ion imaging of the state-selected N_2 fragments, and the nascent rotational distribution of N_2 was deduced from the REMPI spectrum. The comparison of the $O(^1D_2)$ translational energy distribution and the N_2 rotational distribution revealed that REMPI of N_2 via the a″ state is state-selectively suppressed via particular rotational states. As Rijs et al. have first pointed out,[21] the rotational levels in the a″ state are energy-shifted, and we found that the reduction of

REMPI intensity occurs via these levels. Thus, the discrepancy between the O atom translational energy distribution and the N_2 rotational distribution is attributed to the perturbation in the a″ state of N_2. The NN−O bond energy was determined to be 3.629(5) eV in fair agreement with the literature. The $A'(^1\Delta)$ and $A''(^1\Sigma^-)$ are responsible for photodissociation of N_2O in this region, where the rotational excitation may be slightly stronger from the A″ state. The translational energy release is slightly lower in 203 nm photodissociation than that in 205 nm photodissociation, due to enhanced rotational excitation of N_2.

Acknowledgment. We dedicate this work to the late Professor Richard Bersohn who pioneered studies on molecular photodissociation dynamics. We thank Dr. Hideki Katayanagi for his contribution in the early stage of this work at the Institute for Molecular Science (IMS) in Okazaki. This work was supported in part by a Grant-in-Aid for scientific research from the Ministry of Education, Culture, Sports, Science, and Technology of Japan (13127204, 14204063, and 15002011).

References and Notes

(1) McLinden, C. A.; Prather, M. J.; Johnson, M. S. *J. Geophys. Res.* **2003**, *108*, D04233.
(2) Morgan, C. G.; Allen, M.; Liang, M. C.; Shia, P. L.; Blake, G. A.; Yung, Y. L. *J. Geophys. Res.* **2004**, *109*, D04305.
(3) Yung, Y. L.; Miller, C. E. *Science* **1997**, *278*, 1778.
(4) Johnson, M. S.; Billing, G. D.; Gruodis, A.; Janssen, M. H. M. *J. Phys. Chem. A* **2001**, *105*, 8672.
(5) Felder, P.; Haas, B. M.; Huber, J. R. *Chem. Phys. Lett.* **1991**, *186*, 177.
(6) Springsteen, L. L.; Satyapal, S.; Matsumi, Y.; Dobeck, L. M.; Houston, P. L. *J. Phys. Chem.* **1993**, *97*, 7239.
(7) Hanisco, T. F.; Kummel, A. C. *J. Phys. Chem.* **1993**, *97*, 7242.
(8) Suzuki, T.; Katayanagi, H.; Mo, Y.; Tonokura, K. *Chem. Phys. Lett.* **1996**, *256*, 90.
(9) Neyer, D. W.; Heck, A. J. R.; Chandler, D. W. *J. Chem. Phys.* **1999**, *110*, 3411.
(10) Neyer, D. W.; Heck, A. J. R.; Chandler, D. W.; Teule, J. M.; Janssen, M. H. M. *J. Phys. Chem. A* **1999**, *103*, 10388.
(11) Teule, J. M.; Groenenboom, G. C.; Neyer, D. W.; Chandler, D. W.; Janssen, M. H. M. *Chem. Phys. Lett.* **2000**, *320*, 177.
(12) Ahmed, M.; Wouters, E. R.; Peterka, D. S.; Vasyutinskii, O. S.; Suits, A. G. *Faraday Discuss.* **1999**, 425.
(13) Eppink, A.; Parker, D. H. *Rev. Sci. Instrum.* **1997**, *68*, 3477.
(14) Chang, B. Y.; Hoetzlein, R. C.; Mueller, J. A.; Geiser, J. D.; Houston, P. L. *Rev. Sci. Instrum.* **1998**, *69*, 1665.
(15) Hashimoto, N. PhD Thesis, The Graduate University for Advanced Studies, 1998.
(16) Bethune, D. S. *Appl. Opt.* **1981**, *20*, 1897.
(17) Wrede, E.; Laubach, S.; Schulenburg, S.; Brown, A.; Wouters, E. R.; Orr-Ewing, A. J.; Ashfold, M. N. R. *J. Chem. Phys.* **2001**, *114*, 2629.
(18) Yonekura, N.; Gebauer, C.; Kohguchi, H.; Suzuki, T. *Rev. Sci. Instrum.* **1999**, *70*, 3265.
(19) Mo, Y. X.; Suzuki, T. *J. Chem. Phys.* **1998**, *109*, 4691.
(20) Hanisco, T. F.; Kummel, A. C. *J. Phys. Chem.* **1991**, *95*, 8565.
(21) Rijs, A. M.; Backus, E. H. G.; de Lange, C. A.; Janssen, M. H. M.; Wang, K.; McKoy, V. *J. Chem. Phys.* **2001**, *114*, 9413.
(22) Katayanagi, H.; Suzuki, T. *Chem. Phys. Lett.* **2002**, *360*, 104.
(23) Chase, M. W. *J. Phys. Chem. Ref. Data* **1998**, 1621.
(24) Yoshino, K.; Freeman, D. E. *Can. J. Phys.* **1984**, *62*, 1478.
(25) Suzuki, T.; Kakimoto, M. *J. Mol. Spectrosc.* **1982**, *93*, 423.
(26) Hanisco, T. F.; Yan, C.; Kummel, A. C. *J. Phys. Chem.* **1992**, *96*, 2982.
(27) Umemoto, H. *Chem. Phys. Lett.* **1999**, *314*, 267.
(28) Hopper, D. G. *J. Chem. Phys.* **1984**, *80*, 4290.
(29) Suzuki, T.; Katayanagi, H.; Nanbu, S.; Aoyagi, M. *J. Chem. Phys.* **1998**, *109*, 5778.
(30) Brown, A.; Jimeno, P.; Balint-Kurti, G. G. *J. Phys. Chem. A* **1999**, *103*, 11089.